| GRANT AGREEMENT No.: 764902<br>Project Acronym: TOMOCON<br>Project title: Smart tomographic sensors for advanced industrial process control | TOMOCON<br>Smart Tomographic Sensors for Advanced Industrial Process Control | |
|---|---|---|
| Deliverable Rel. No.<br>**D5.3.** | Lead Beneficiary<br>**TUD** | |
| EU Del. No.<br>**D17** | Type<br>**Report** | |
| WP No.<br>**WP5** | Date:<br>**29.10.2019** | Revision:<br>**0** |

**Innovative Training Network**

**TOMOCON**

Deliverable Title

# Virtual Demonstration Results

Description

**This deliverable describes the results of the virtual demonstrations for all four demonstration cases.**

| | | |
|---|---|---|
| Prepared by: | Dr. Luis Portela | Luis Portela |
| Approved by: | Prof. Dr. Uwe Hampel | U. Ha |
| Approved by Supervisory Board: | | **30.10.2019** |

Dissemination Level: **Public**

*This project has received funding from the European Union's Horizon 2020 research and innovation programme under the Marie Skłodowska-Curie Grant Agreement No. 764902.*

Revision Sheet

| Revision Number | Purpose of Revision | Effective Date |
|---|---|---|
| 0 | Initial Issue | 30.10.2019 |
| | | |
| | | |
| | | |




*This project has received funding from the European Union's Horizon 2020 research and innovation programme under the Marie Skłodowska-Curie Grant Agreement No. 764902.*

## Table of Contents





*This project has received funding from the European Union's Horizon 2020 research and innovation programme under the Marie Skłodowska-Curie Grant Agreement No. 764902.*

*This project has received funding from the European Union's Horizon 2020 research and innovation programme under the Marie Skłodowska-Curie Grant Agreement No. 764902.*

# Virtual Demonstration Results

# 1. Inline Fluid Separation

## 1.1. Brief introduction to our system

The core radius over time at the pickup tube location is calculated via the Lagrange tracking of the particles (oil droplets / air bubbles) along the flow, using the ERT measurement over time as the initial condition of their motion.

The control strategy is based on the tracking of the extrapolation of the core radius to a location close to the pickup tube. It is assumed that the flow split effects create a region where the particles are collected, and this region is concentric in relation to the pipe's wall. The growth of this region is related to the mass balance of the area, determined by a fixed flow rate at its upstream side and the flow split at its downstream side.

The flow split as a function of time is given by a PID controller in a feedback loop, in which the error used to calculate its response is given by the difference between the prediction of the area contained by the particle position and the area currently being captured by the pickup tube. The idea is that the controller adjusts the flow split to overlap the two regions, leading to a perfect separation of the phases in the context of the model, i.e., all the heavy phase is going to the heavy phase outlet, while the entire light phase crosses the pickup tube.

For more detailed information on the control loop and the equations, please refer to Deliverable 4.2.

### 1.1.1. System of equations

In Deliverable 4.2., a transfer function representation of the loop was presented. The loop was modified to a state-space (discrete) representation for the demonstration itself, allowing an easy change in the reference over time, being fitted directly from the ERT measurements.

The plant is given by:

$$\frac{d\phi}{dt} = A(\phi - FS) \qquad (1)$$

Where $\phi$ represents the percentage of the total area currently being captured, and *FS* is the flow split itself. As mentioned in the previous section, the balance of mass determines the growth of the region, and *A* is a constant relation of its volume with the pipe area.

The controller is based on the error via a PID approach. As mentioned, the error is given by:

$$e = \frac{R^2_{predicted}}{R^2} - \phi \qquad (2)$$

Leading to:

$$FS(t) = K_p e + K_i \int e dt + K_d \frac{de}{dt} \qquad (3)$$



*This project has received funding from the European Union's Horizon 2020 research and innovation programme under the Marie Skłodowska-Curie Grant Agreement No. 764902.*

At this point, it is worth mentioning that the predicted position is delayed in relation to the measurement due to the transport of the particles by the flow, and the integral and derivative values of the error are evaluated numerically.

### 1.1.2. Time response and stability

The adoption of the frequency of measurements of the ERT sensor to the control loop itself leads to a total instability of the system. Therefore, the measurements of the ERT are assumed as being constant (zero order hold) until a new value is obtained, and the control loop itself works at a higher frequency than the sensor itself.

## 1.2. Interface built for the virtual demonstration

A Graphical User Interface (GUI) was built for the demonstration inside MATLAB. A picture of the GUI is presented in Figure 1.

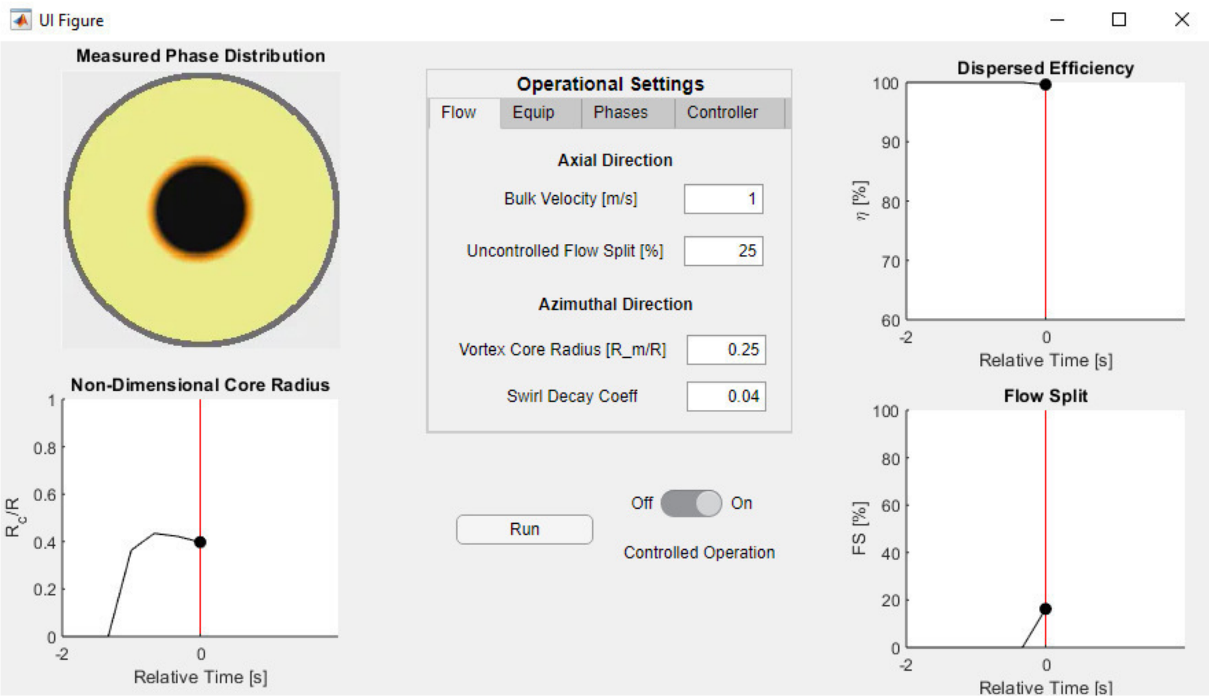


**Figure 1:** Graphical User Interface built for the virtual demonstration

There are no pre-calculated parameters inside the interface code. It fits the core in real time, based on the video playing at the top left corner. In a real application, the reconstructed flow profile by the ERT is used instead of the video. The video is played at 3 Hz, mimicking the sensor itself.

The fitted value is plotted over time in the graph at the bottom left corner, that keeps moving so the values are always plotted in the central position of the graph, evidenced by the red line in it.



*This project has received funding from the European Union's Horizon 2020 research and innovation programme under the Marie Skłodowska-Curie Grant Agreement No. 764902.*

The mid panel allows the setting of different parameters of the flow and of the controller constants. These values are used to predict the particle's path, and can be freely modified by the user. The parameters that can be changed are:

- Flow Tab:
  - The bulk velocity inside the separator
  - The initial flow split of the flow
  - The gas core radius
  - The swirl decay coefficient over the length
- Equipment Tab:
  - The angle of the vanes of the swirl element
  - The slip coefficient of the flow in relation to the vane angle
  - The swirl tube length
  - The swirl tube diameter
- Phases Tab:
  - The density of the continuous phase
  - The viscosity of the continuous phase
  - The density of the dispersed phase
  - The diameter of the dispersed phase
- Controller Tab:
  - The values of Kp, Ki and Kd

The initial values originally presented in the code are recommended as they were selected based on previous tests.

The switch placed below the panel allows to set the response to controlled or non-controlled, in order to check the impact of the controlled operation in the efficiency of separation (top right graph) and the flow split over time imposed by the controller (bottom right graph).

### 1.3. Conditions adopted

The presence of small oil particles in a water medium was chosen for the virtual demo due to the slower motion of these elements in relation to gas particles, that are quickly dragged to the center of the pipe. The conditions adopted during the virtual demonstrations are presented over the different tabs of the mid panel in Figure 2.

These conditions correspond to the flow rate, the swirl element, and the dimensions similar to the real setup used in the final demonstration of the project. Also, the coefficients and the vortex size are values commonly found in literature.



*This project has received funding from the European Union's Horizon 2020 research and innovation programme under the Marie Skłodowska-Curie Grant Agreement No. 764902.*

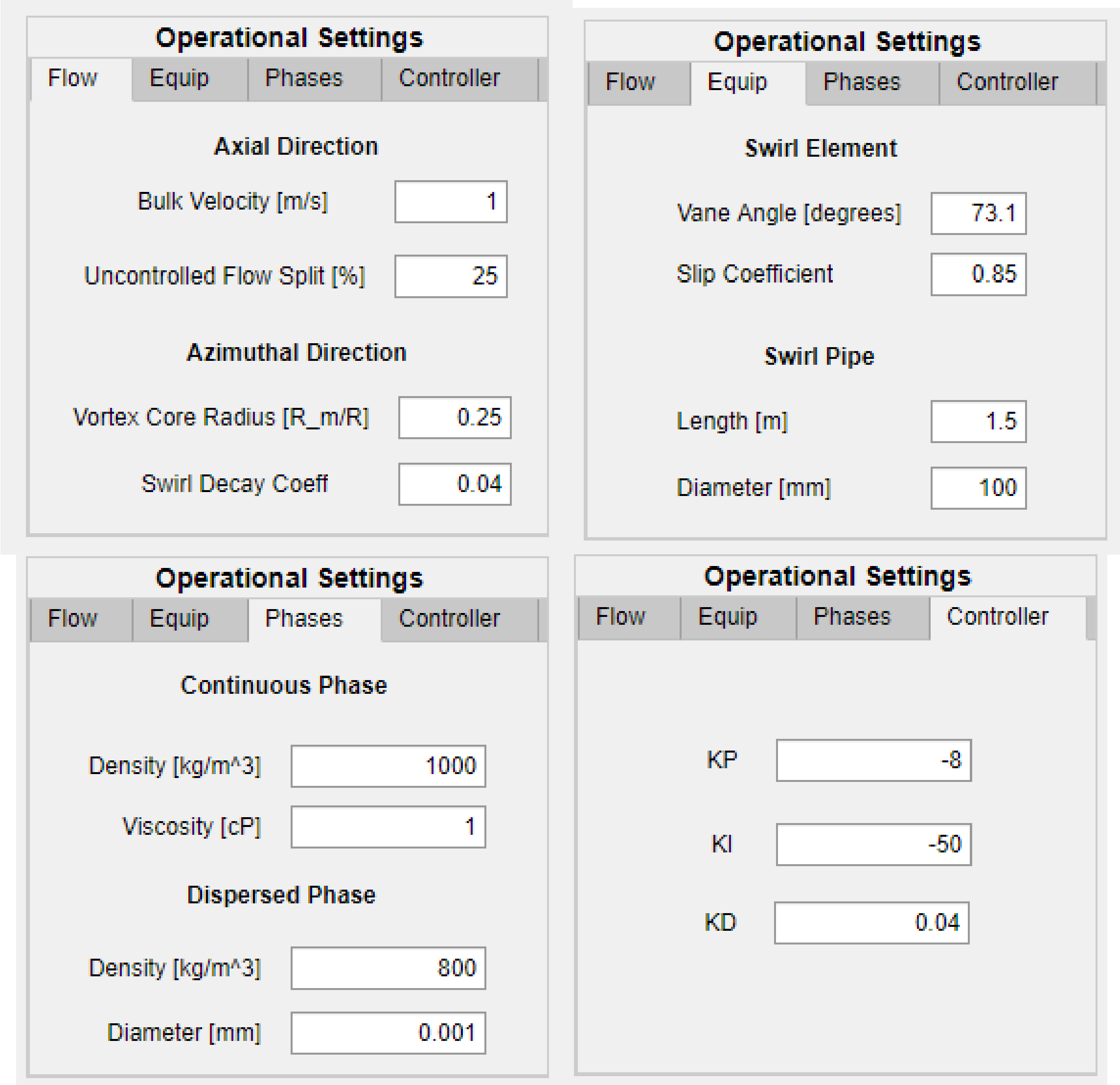


**Figure 2:** Different tabs of the settings panel used in the virtual demonstration

## 1.4. Results and discussion

### 1.4.1. Gain in efficiency

Figure 3 presents a comparison of the efficiency of the controlled against the uncontrolled operation of the setup. It is notable that the controlled version of the setup presents a huge gain in efficiency. The dispersed efficiency values were increased from around 75 %, with oscillations of more than 20 % to an almost fixed value of 100 %, for the conditions presented in Figure 2.

It is worth mentioning that the gain in efficiency occurs for the uncontrolled condition when the core size naturally approaches the region being captured by the valve, due to a change




*This project has received funding from the European Union's Horizon 2020 research and innovation programme under the Marie Skłodowska-Curie Grant Agreement No. 764902.*

in the upstream conditions (before the equipment) present in the video, and presents an intrinsically random behavior.

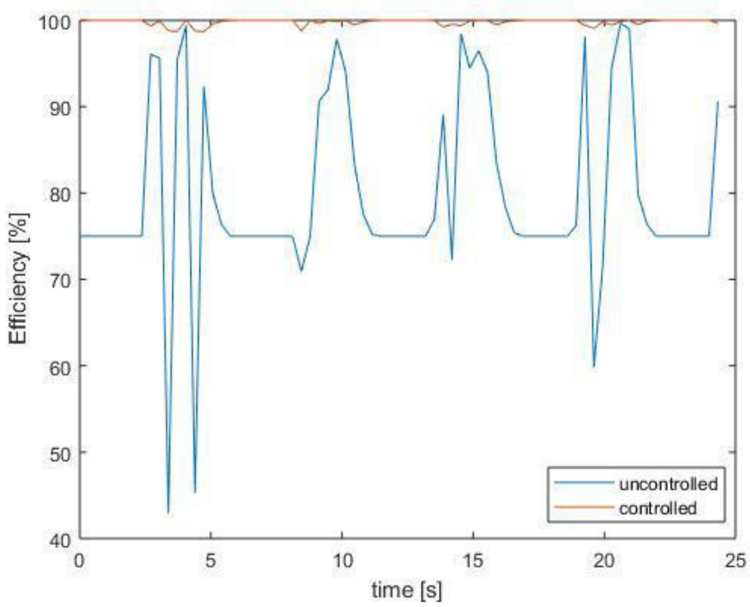


**Figure 3:** Impact of the control action in the efficiency of separation

The gain in the efficiency of the separator for the controlled operation is obtained for every scenario considered, which is deeply related to the model chosen to represent the flow. Once a sufficient time resolution and reasonable constants for a stable control are achieved, the controlled results will always be better than the uncontrolled one. However, this is not what we expect for a real flow.

The change in the valve opening can lead to instabilities in the flow distribution inside the pipe, and the model chosen to represent the action of the valves is not totally reliable, especially when considering the zero-order hold of the flow profile between two measurements. Also, the presence of a reverse flow is not represented in the model, which greatly impacts the efficiency, and the predictability of the particle position in the pickup tube.

Therefore, in order to achieve a more realistic model of the separator, a better understanding of the physics of swirling flows is required. The use of discretized elements along the pipe as states, together with a more reliable flow velocity profile, are good alternatives to achieve more realistic results.

### 1.4.2. The overshooting behavior of the valves

The PID controller, as implemented, leads to a huge stress in the valve, due to abrupt changes in its opening and overshoots. This is especially related to changes in the reference conditions, that, due to the zero order hold, act as a sequence of steps. The behavior of the values can be seen in Figure 4.




*This project has received funding from the European Union's Horizon 2020 research and innovation programme under the Marie Skłodowska-Curie Grant Agreement No. 764902.*

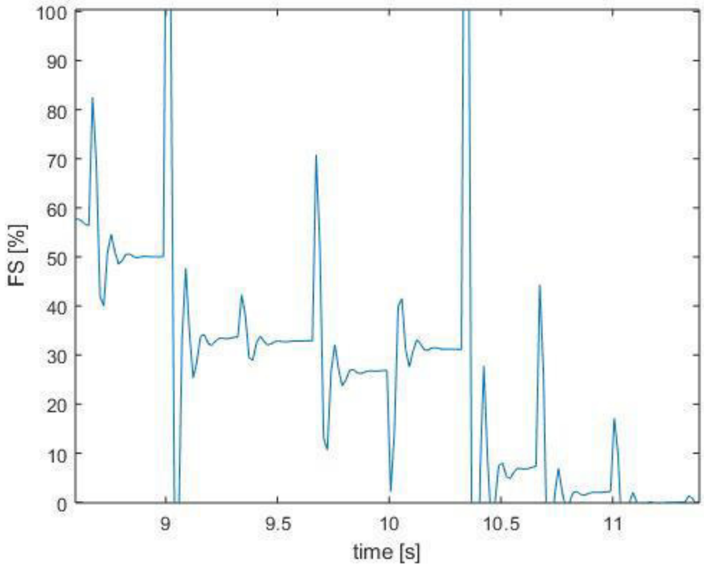


**Figure 4:** Flow split over time for the conditions explored

The existence of overshooting in the PID system is related to the requirement of a fast response that does not allow the use of a critically damped / overdamped system.

A MPC approach could be used to improve the efficiency of capturing the core without this overshoot of the valves, especially in the transition between the two measurements of the ERT sensor. As the approach also takes the limitations of the system into account, the rate of change in the valve positions can be limited to a region that maximizes the life of such elements.

## 1.5. Conclusions

A simplified model of the controlled separator was developed, and a GUI was built to check its response. The results obtained show that (i) a deeper understanding of the physics of the flow is required, as the current model presents an oversimplified response in relation to the real flow inside the separators, and (ii) a MPC controller should be used to eliminate the overshoots of our system, and to minimize the stresses in the valves of the setup. Moreover, the use of a MIMO system, naturally present in the MPC, instead of the current SISO one allows changes in multiple elements (in our case the valves at the two outlets) which is also beneficial for our system; the flow is more sensible to changes in multiple elements, which allows a smaller change in each of the valves for the same response of the system, thereby increasing their lifetime.



*This project has received funding from the European Union's Horizon 2020 research and innovation programme under the Marie Skłodowska-Curie Grant Agreement No. 764902.*

# 2. Microwave Drying

## 2.1. Introduction

The drying of dielectric materials is one of the common processes in several industries. Among the main objectives of this process are reaching a best possible uniform moisture distribution inside the material and reducing the energy consumption and processing time. The microwave heating technology makes the volumetric and selective heating possible. To benefit from its features, an advanced control system is developed to determine the power levels of the distributed microwave sources (UEF, ESR 14). However, the moisture distribution of the material which is an impregnated foam in our case as well as a process model are required to derive this controller. An ECT sensor (UEF, ESR 14) and a MWT sensor (UEF, ESR 15; KIT, ESR 7), are developed to reconstruct the material permittivity which strongly correlates with the moisture content. Additionally, a mathematical model for describing the heat and mass transfer inside the foam is developed to design the model-based controller (UEF, ESR 14).

Besides, in this demonstration we benefit from deep learning and human computer interaction visualization for several purposes (CTH, ESR 3). One main advantage can be analyzing the output images from ECT and MWT using deep learning to identify the moisture locations.

All the components in this project have been connected using MATLAB software to run the virtual demonstration. Fig. 5 shows the SIMULINK schematic. The controller, specified by the green color, determines the power levels of the microwave sources having the moisture distribution information and the desired moisture level. Given the power levels as inputs, the process model calculates the moisture and temperature distribution inside the foam. In this virtual demonstration, these are the true distributions. However, in practice, the moisture distribution should be reconstructed using either ECT or MWT sensors. The temperature distribution on the surface of the foam can be measured with an infrared camera. In the virtual demonstration, the ECT and MWT sensors are connected to the process model. They receive the true moisture distribution and by solving the forward problem, the corresponding measurements are calculated. This way, we will have synthetic measurements related to the current moisture state of the foam. The sensors will reconstruct the foam permittivity distribution, which in turn will be converted to the moisture information through a mapping. The resulted moisture distribution will then be fed to the controller. The rest of section 2 describes each component of the virtual demonstration in more detail and at the end, the results of the closed loop simulations are given.



*This project has received funding from the European Union's Horizon 2020 research and innovation programme under the Marie Skłodowska-Curie Grant Agreement No. 764902.*

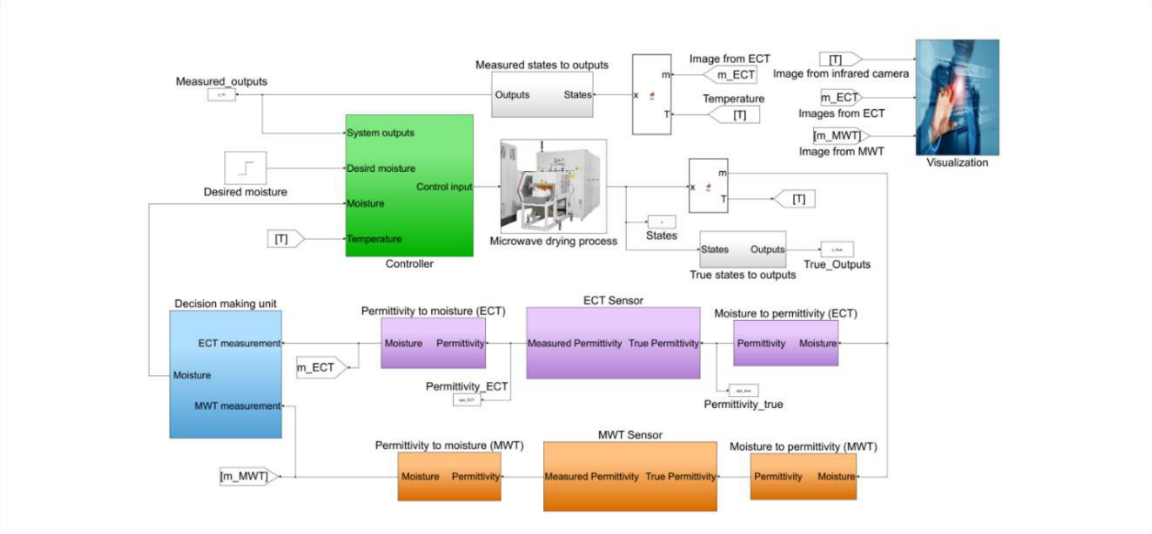


**Figure 5:** System schematic

## 2.2. Process modelling

The microwave drying process is a very complicated process consisting of momentum conservation, mass conservation and energy conservation. We need a simple yet efficient model to describe the heat and mass transfer in the foam portion inside the cavity because the complexity of the model can result in a difficulty in the computations and in the design of the controller.

To describe the heat and mass transfer in the foam inside the cavity, the proposed coupled partial differential equations (PDEs) for the mathematical description of the heat and mass transfer in capillary-porous bodies are modified and extended to model the microwave drying process. These equations are

$$\frac{\partial}{\partial t}\left[\frac{\rho M}{100}\right] = \vec{\nabla}\cdot\left[\left(\frac{k_m \delta}{c_m}\right)\nabla T + \frac{k_m}{100 c_m}\vec{\nabla} M\right], \tag{4}$$

$$\frac{\partial}{\partial t}\left[\rho c_q T\right] = \vec{\nabla}\cdot\left[\left(k_q + \frac{\mu\lambda k_m \delta}{c_m}\right)\nabla T + \frac{\mu\lambda k_m}{100 c_m}\vec{\nabla} M\right] + P_{mw}^{n} u, \tag{5}$$

where $M$ is the moisture content percentage, $T$ is the temperature, $k_m$ is the moisture conductivity, $k_q$ is the thermal conductivity of the material, $c_m$ is the moisture capacity, $c_q$ the heat capacity, $\delta$ is the thermal gradient coefficient, $\rho$ is the density, $\lambda$ is the latent heat of vaporization, and $\mu$ is the ratio of the vapor diffusion coefficient to the coefficient of the total moisture diffusion.





*This project has received funding from the European Union's Horizon 2020 research and innovation programme under the Marie Skłodowska-Curie Grant Agreement No. 764902.*

The last term in Eq. (5) describes the effect of microwave heating. The boundary conditions for the PDEs (4)-(5) are described by

$$-k_q\frac{\partial T}{\partial n} = h_q\left(T - T_g\right) + \frac{(1-\mu)\lambda h_m}{100c_m}\left(M - M_g\right), \tag{6}$$

$$\frac{-k_m}{100c_m}\frac{\partial M}{\partial n} = \left(\frac{k_m\delta}{c_m}\right)\frac{\partial T}{\partial n} + \frac{h_m}{100c_m}\left(M - M_g\right), \tag{7}$$

where $h_q$ is the convective heat transfer coefficient, $h_m$ is the convective mass transfer coefficient, $M_g$ is the bulk gas moisture content and $T_g$ is the bulk gas temperature.

The equations (4)-(7) are discretized and solved in 2D / 3D using the Finite Element Method (FEM). Computing the microwave heating power $P_{mw}^n$ requires the information of the electric field and this information is calculated using COMSOL Multiphysics.

Discretizing the model results in a system of ordinary differential equations (ODEs) where each of them describes the moisture or temperature at each node. From this system of ODEs, the discrete-time state space model can be written as

$$x(k+1) = Ax(k) + Bu(k) \tag{8}$$

$$y(k) = Cx(k) \tag{9}$$

where

$$x(k) = [M(k) \quad T(k)]^T \tag{10}$$

$$u(k) = [u_1 \quad u_2 \quad u_3 \quad u_4 \quad u_5 \quad u_6]^T \tag{11}$$

and matrices $A$ and $B$ are obtained using FEM. Here, $x$ is the state vector including the moisture and the temperature at each node, $u$ is a vector that indicates the power level of each microwave source, $y$ is the measured system output, and $k$ refers to time. In this demonstration, there are six microwave sources; however, they can be extended to a greater number of sources in the lab demonstration. Besides, it is assumed that the moisture and temperature information inside the foam is available. Therefore, the matrix $C$ in equation (9) is an identity matrix. In the lab demonstration, a Kalman filter will be used to estimate the unavailable states.

The model parameters are given in Tab. 1. At this point, these parameters are taken from a wood sample since there is no information available for the foam. In the lab demonstration, values for the foam will be used.



*This project has received funding from the European Union's Horizon 2020 research and innovation programme under the Marie Skłodowska-Curie Grant Agreement No. 764902.*

**Table 1:** Model parameters

| Parameter | Unit | Value |
|---|---|---|
| $c_q$ | $\mathrm{J\,kg^{-1}\,K^{-1}}$ | 1400 |
| $\rho$ | $\mathrm{kg\,m^{-3}}$ | 416 |
| $k_q$ | $\mathrm{W\,m^{-1}\,K^{-1}}$ | 0.16 |
| $\lambda$ | $\mathrm{J\,kg^{-1}}$ | $2.5 \times 10^{6}$ |
| $h_q$ | $\mathrm{W\,m^{-2}\,K^{-1}}$ | 15 |
| $h_m$ | $\mathrm{M\,s^{-1}}$ | $6 \times 10^{-5}$ |
| $\delta$ | $\mathrm{kg_{moisture}\,kg^{-1}K^{-1}}$ | 0.025 |
| $\mu$ | - | 0.3 |
| $k_m$ | $\mathrm{kg_{moisture}}\,\mathrm{m}^{-1}s^{-1}\mathrm{M}^{-1}$ | $1.8 \times 10^{-8}$ |
| $c_m$ | $\mathrm{kg_{moisture}\,kg^{-1}M^{-1}}$ | 0.01 |
| $T_g$ | K | 373 |
| $M_g$ | 5 | % |

## 2.3. Controller

The controller for the microwave drying system is developed using the Linear Quadratic Regulator (LQR) control method. The controller is designed based on the multi-input multi-output model of the process and the control objective is to track a desired moisture level. Fig. 6 shows the structure of this controller. The matrices $A$, $B$, and $C$ are from the process model given in equations (8-9).

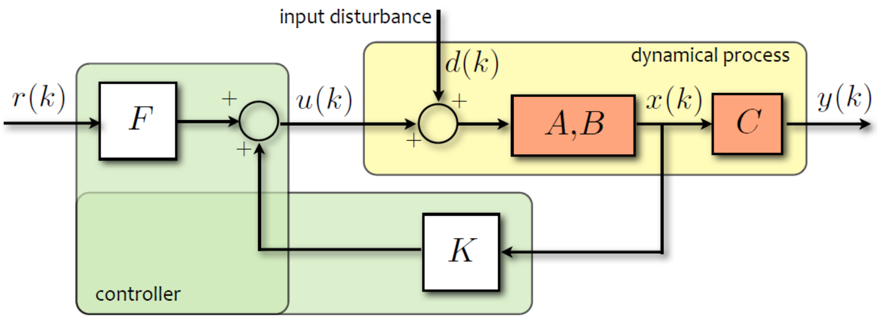


**Figure 6:** Structure of the controller



*This project has received funding from the European Union's Horizon 2020 research and innovation programme under the Marie Skłodowska-Curie Grant Agreement No. 764902.*

The control law in this structure is

$$u(k) = -Kx(k) + Fr(k), \tag{12}$$

where $K$ is the controller gain calculated using the LQR control method, $r(k)$ is the desired moisture level and $F$ is a constant gain which is chosen by trial and error such that it ensures reference tracking.

To calculate the controller gain $K$, an optimization problem needs to be solved. The goal is to minimize the cost function

$$J = \sum_{k=0}^{\infty} x(k)^T Qx(n) + u(n)^T Ru(n), \tag{13}$$

where $Q$ and $R$ are design matrices and are chosen such that $R > 0$ and $Q \geq 0$. The relative values of these matrices affect the speed of state convergence and the magnitude of the control efforts. To minimize this cost function in an infinite time horizon, the following algebraic Riccati equation should be solved

$$S = A^T SA - A^T SB(R + B^T SB)^{-1} B^T SA + Q, \tag{14}$$

where $S$ is the solution of the Riccati equation. The controller gain is then calculated as

$$K = (R + B^T SB)^{-1} B^T SA \tag{15}$$

Having calculated the control gain, the control law (12) can be derived.

## 2.4. Sensors

### 2.4.1. Permittivity to moisture mapping

Both sensors, ECT and MWT, reconstruct the permittivity distribution inside the foam. However, the required information by the controller is the moisture distribution. Therefore, a mapping from the permittivity to moisture distribution is needed. This mapping is also influenced by the temperature of the foam and the frequency. Since the ECT and MWT sensors work at different frequencies, different mappings for these sensors should be employed. However, at this point only one mapping is available and both sensors in this virtual demonstration use the same. The mapping from the moisture percentage to the real part of the permittivity is as

$$\epsilon_r = a \exp(b\, M), \tag{16}$$

where $a$ and $b$ are the mapping constants, $\epsilon_r$ is the real part of the relative permittivity, and $M$ is the moisture percentage. Besides, to run the virtual demonstration and test the sensors, they receive the true moisture distribution from the process model, and they need to solve the forward problem to acquire the corresponding measurements. To do this, the corresponding permittivity to the true moisture distribution is required and the inverse of the mapping (16) is used to obtain this information.



*This project has received funding from the European Union's Horizon 2020 research and innovation programme under the Marie Skłodowska-Curie Grant Agreement No. 764902.*

### 2.4.2. ECT sensor

The ECT sensor consists of several electrodes mounted around the target. By applying an electrical voltage to one of the electrodes, the electrical capacitances between the other electrodes are measured. By repeating this measurement procedure and having each of the electrodes as a source, the electrical permittivity of the target can be reconstructed. To design this sensor for the microwave drying process, an algorithm to solve the inverse and the forward problem is developed. The forward problem is solved using the FEM while the difference imaging method is employed to solve the inverse problem. Then, the number and the configuration of the electrodes of the sensor are determined by designing and simulating different configurations. These configurations are designed using MATLAB / NETGEN. Fig. 7 shows the final design of this sensor consisting of 12 electrodes. 6 electrodes are mounted on the top surface and 6 electrodes on the bottom surface. There are no electrodes on the sides since they do not have a significant contribution to the reconstruction results.

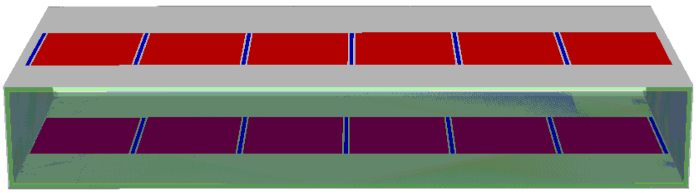

**Figure 7:** The ECT sensor configuration

### 2.4.3. MWT sensor

Microwave tomography (MWT) is a technique of estimating the material properties of an object from the measured data of the scattered electromagnetic field. An antenna array is used to measure the scattered electric field in terms of S-parameter which is then given as an input to a reconstruction algorithm for recovering the moisture content distribution. For our present microwave drying system employing a conveyor belt and a large sample size under drying, the speed by which the moisture distribution information will be available from the MWT is crucial. As a result, a proper inversion algorithm should be chosen alongside with the type and number of antennas for fulfilling the demand for fast reconstruction. Targeted are 10 Hz acquisition speed for bimodal measurement and $< 1$s latency. A MWT model with simple dipole antennas operating at 3 GHz frequency is developed in COMSOL as shown in Fig. 8.



*This project has received funding from the European Union's Horizon 2020 research and innovation programme under the Marie Skłodowska-Curie Grant Agreement No. 764902.*

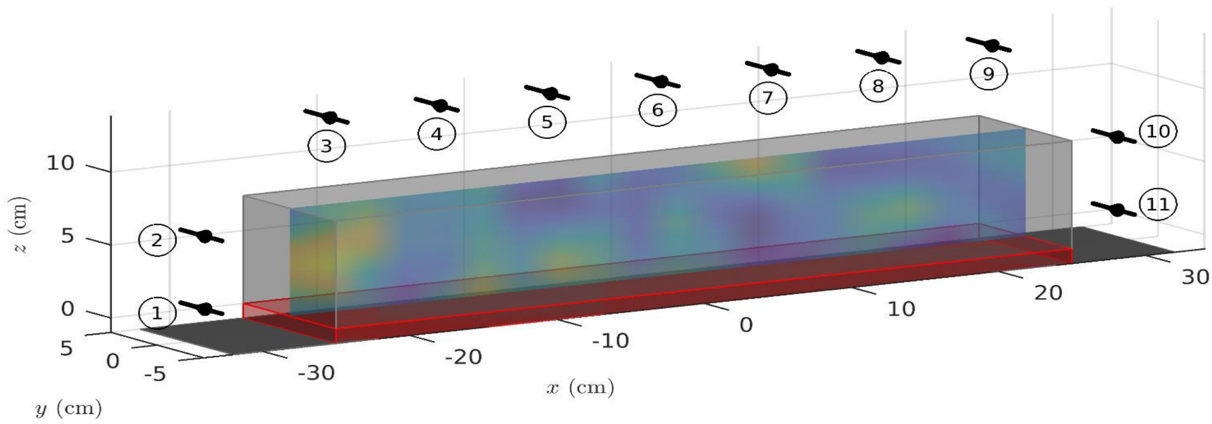


**Figure 8:** Model of MWT used for benchmarking purposes. The light gray box is the porous foam (color surface inside the porous foam illustrates the potential moisture) and the red box the conveyor belt while the dark gray surface denotes the perfect electric conductor (PEC) boundary. The antenna array is visualized with black cylinders.

The FEM is chosen to simulate the electromagnetic wave propagation (forward model) while a deep learning technique is used to estimate the moisture distribution of a porous foam from the measured scattered electric field data. In our present study, the neural network is trained with different moisture sample scenarios and their associated scattered electric field data from the COMSOL simulation. The moisture samples, modelled as Gaussian random fields, are based on the laboratory measurements (Karlsruhe Institute of Technology, Institute for Pulsed Power and Microwave Technology, Germany) by which the mathematical relation between the moisture content and the complex permittivity $\varepsilon = \varepsilon' - i\varepsilon''$ is known with acceptable accuracy. This relation can be used to recover the physical parameters from the sampled moisture content distribution.

A neural network is trained to map from the moisture content distribution to the scattered field. The network architecture used in this work comprises two convolution layers and two fully connected layers. For the training of the neural network, we generated a dataset comprising 15,000 moisture samples. The real and imaginary part of the complex-valued measurement data, i.e. S-parameter, is vectorized and given as an input to the neural network.

The scattered field for the corresponding input moisture samples coming from the drying process are calculated and fed to the trained neural network to estimate the moisture content.

### 2.4.4. Decision making unit

The ECT and MWT sensors both measure the moisture information inside the foam. The controller only requires the moisture information from one of those. A decision-making unit decides to transfer data from either ECT or MWT. This unit can be simply a switch.




*This project has received funding from the European Union's Horizon 2020 research and innovation programme under the Marie Skłodowska-Curie Grant Agreement No. 764902.*

## 2.5. Human computer interaction

The controller concept shall incorporate knowledge-based control and self-learning by making use of a data repository for different goods, geometries and process parameters. Expertise should be brought in the design and analysis of advanced human-machine interfaces with the treatment of 4D data. At the far end, the Internet of Things will provide a connectivity tool between multiple tomographic sensor systems. Novel visualizations should be carried out by making use of the process data. Two different tasks are defined within this demonstration which are described as follows.

**Task 1:** In our demonstration, we proposed an automatic state-of-the-art segmentation method--MWTS-KM--to visualize the low moisture area in the MWT and ECT images. Fig. 9 is an example of a reconstructed tomographic image, and Fig. 10 shows the pipeline of the MWTS-KM method. The segmentation algorithm is implemented for both MWT and ECT images and the results are shown in section 2.6.

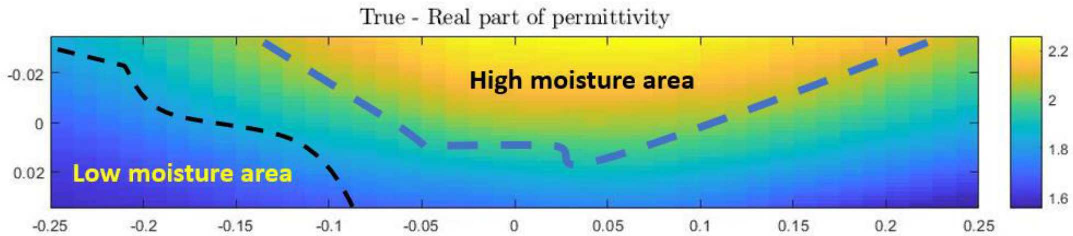


**Figure 9:** Example of MWT image

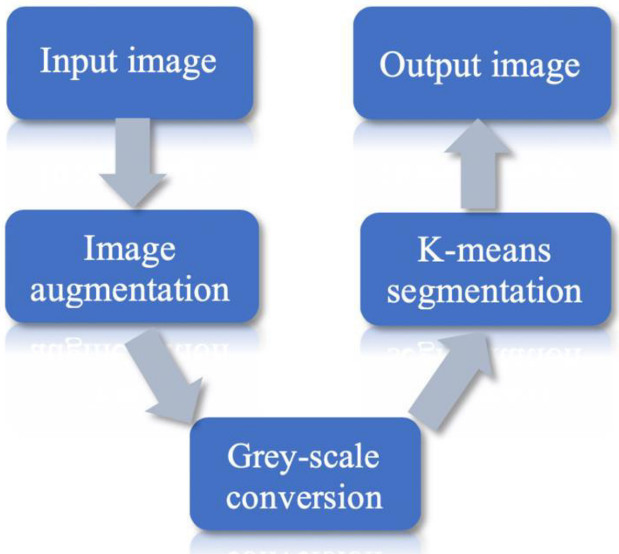


**Figure 10:** The pipeline of the proposed MWT Segmentation based on K-means (MWTS-KM) algorithm





*This project has received funding from the European Union's Horizon 2020 research and innovation programme under the Marie Skłodowska-Curie Grant Agreement No. 764902.*

**Task 2:** Microwave drying process condition monitoring via infrared images. The areas of high moisture and low moisture could be detected precisely to find the faults. This work enables us to be eligible to observe the drying process taking place in an isolated chamber (Beneficiaries: CTH, KIT). This task is not done in this virtual demonstration.

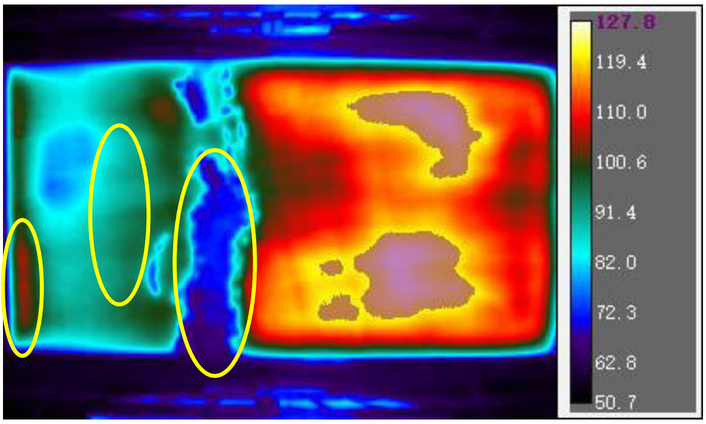


**Figure 11:** Example of an infrared image with different moisture levels

## 2.6. Results and discussion

In this section, the simulation results from the closed loop operation are demonstrated. The foam sample has an initial homogenous moisture content of 80 %. The objective is to reach the desired moisture level. In this simulation, 15 % moisture content is chosen as the desired value.

The LQR controller determines the power level of the microwave sources, such that the moisture content of the foam sample reaches the desired level. The average moisture and temperature of the sample under the LQR controller are shown in Fig. 12. As seen, the average moisture converges to the desired level very accurately. The average temperature also reaches the gas temperature at the steady state.





*This project has received funding from the European Union's Horizon 2020 research and innovation programme under the Marie Skłodowska-Curie Grant Agreement No. 764902.*

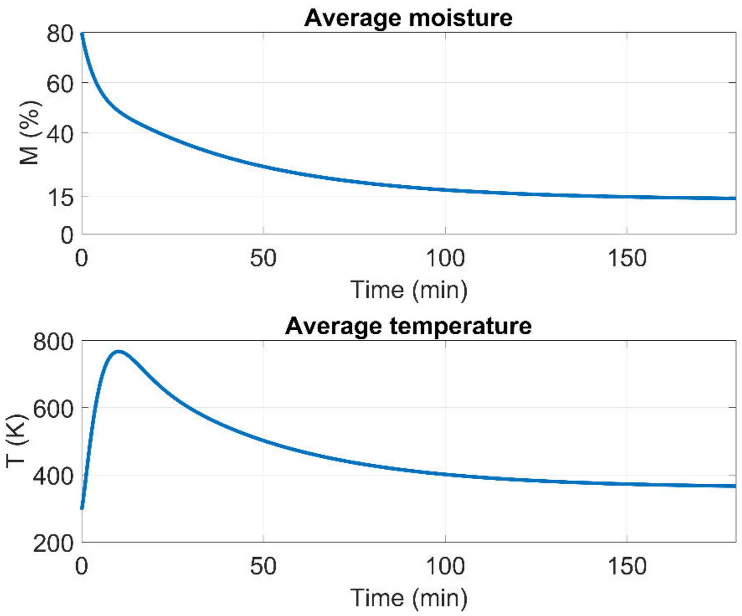


**Figure 12:** Average moisture and temperature of the sample during the drying process

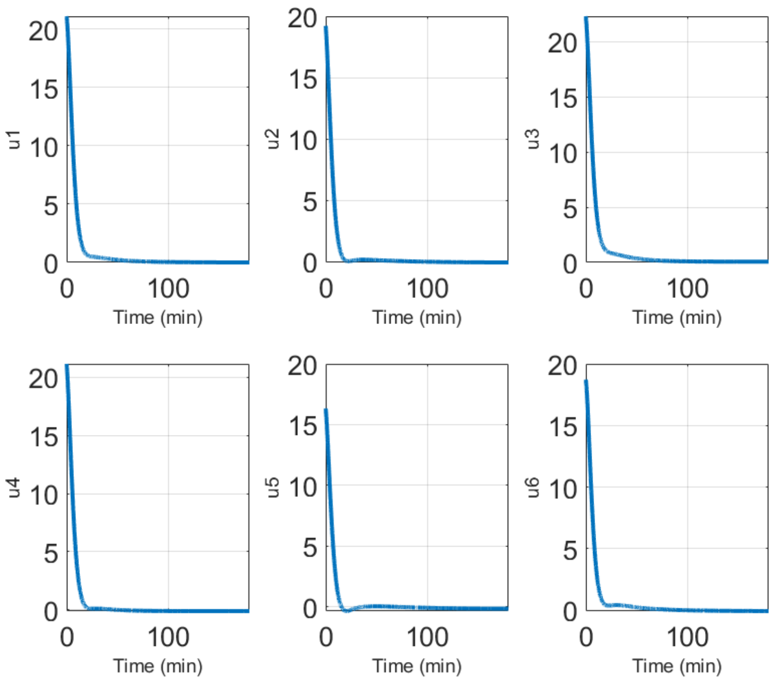


**Figure 13:** Control efforts command by the LQR controller during the drying process

Fig. 13 shows the control effort commanded by the LQR controller. The control inputs here are the power levels of the microwave sources. Level 1 corresponds to the maximum power of each source which is assumed to be 2 kW. However, as shown in this figure, the control





*This project has received funding from the European Union's Horizon 2020 research and innovation programme under the Marie Skłodowska-Curie Grant Agreement No. 764902.*

effort at the transient time is more than 1 which means that the system needs more than the maximum power of that source. This is because the LQR control cannot satisfy constraints over the control input. Therefore, it can command more than the allowed power level. This issue will be resolved in further demonstrations by employing more advanced control techniques such as Model Predictive Control (MPC).

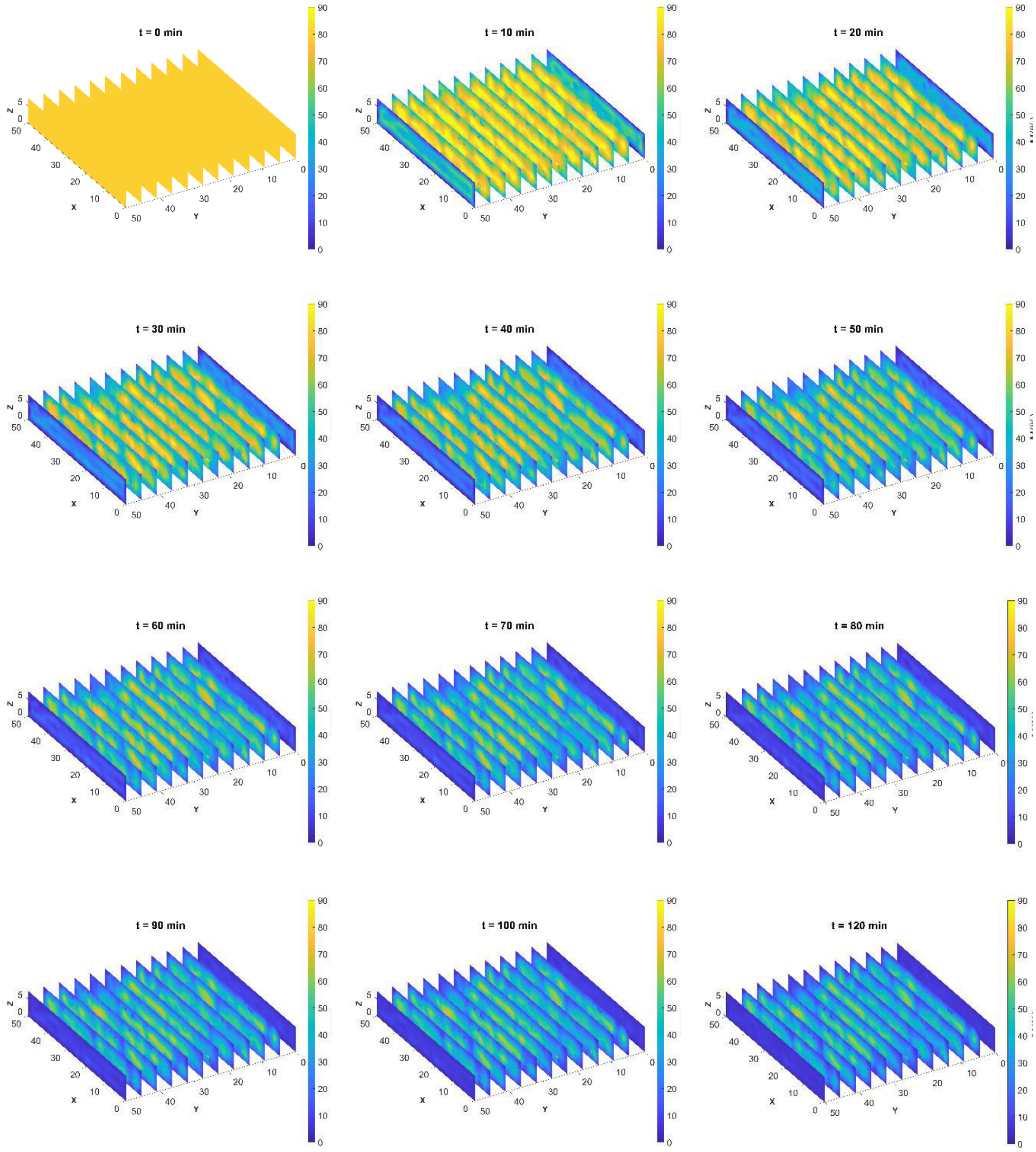


**Figure 14:** Moisture distribution inside the sample during the drying process at different time steps





*This project has received funding from the European Union's Horizon 2020 research and innovation programme under the Marie Skłodowska-Curie Grant Agreement No. 764902.*

The goal in the microwave drying process is not only achieving a desired average moisture content. The moisture distribution is also important, and the goal is to reach a moisture distribution as homogenous as possible. Fig. 14 shows the moisture distribution of the sample during the drying process. As seen, it starts with a homogenous moisture of 80 % at $t = 0$ and then gradually the moisture content reduces over time. The surrounding gas moisture is assumed to be 5 %, so the moisture transfer at the boundary surfaces is faster than the inner layers.

Fig. 14 shows the moisture distribution calculated by the model. However, the moisture information should be obtained through either the ECT or MWT sensors. The moisture reconstruction algorithms for both sensors, which consist of solving the forward and inverse problems, are employed to measure the moisture distribution. Both sensors reconstruct the 2D moisture distribution to save the computation time. To have a better comparison between these sensors, the reconstruction results of both sensors together with the true moisture distribution from the model at different time steps are demonstrated in Fig. 15. As shown, the results of the reconstruction for both sensors are very close to the true distribution and are completely satisfying. In the MWT sensor, the nonlinear inverse problem is solved using a fast neural network approach while in the ECT, a fast one-step algorithm is employed to solve the linearized problem. Therefore, the values of the distribution with MWT are closer to the true values than with ECT. However, in terms of identifying the distribution, both sensors work very well.



*This project has received funding from the European Union's Horizon 2020 research and innovation programme under the Marie Skłodowska-Curie Grant Agreement No. 764902.*

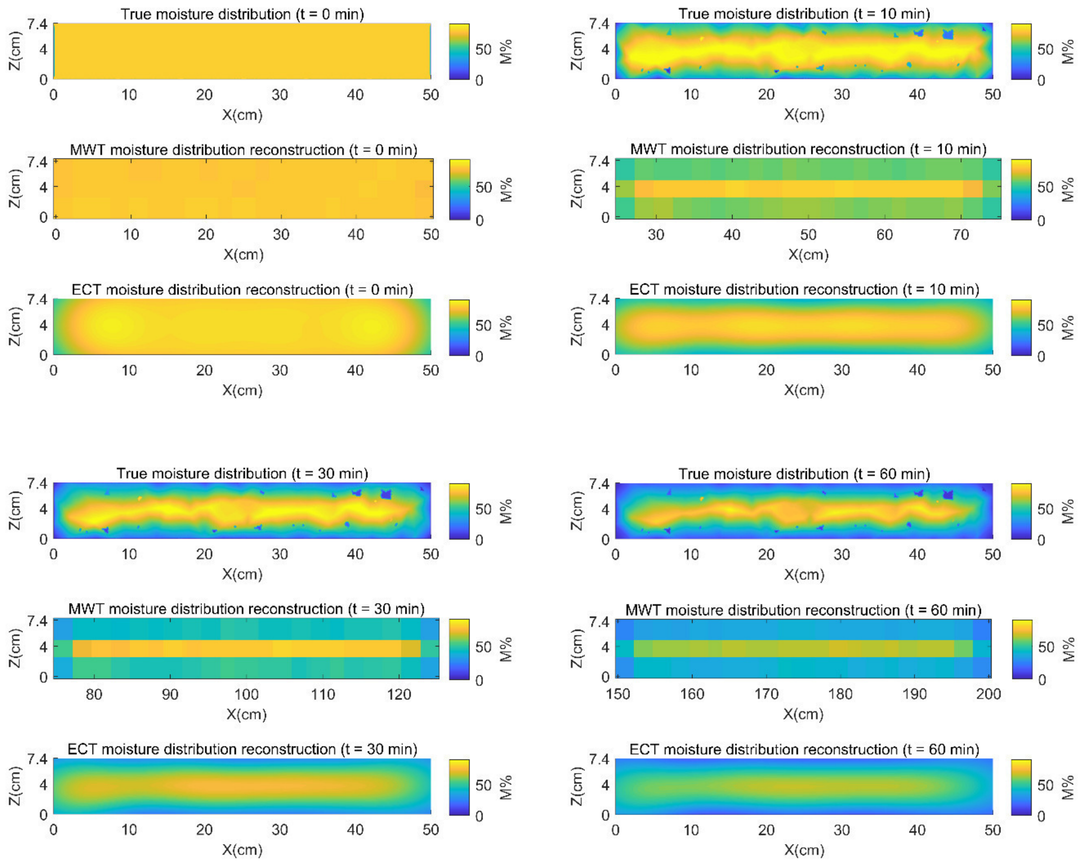


**Figure 15:** Moisture reconstruction using a MWT and an ECT sensor during the drying process at different time steps

The visualization of microwave drying is a task which can work in parallel to the closed loop operation of the system and provides information for the operator. As the first possible task for the visualization, the image segmentation is done for ECT and MWT images at different time steps and the results are shown in Fig. 16 and Fig. 17. The black parts are the low moisture areas which are the desirable results we aim for.




*This project has received funding from the European Union's Horizon 2020 research and innovation programme under the Marie Skłodowska-Curie Grant Agreement No. 764902.*

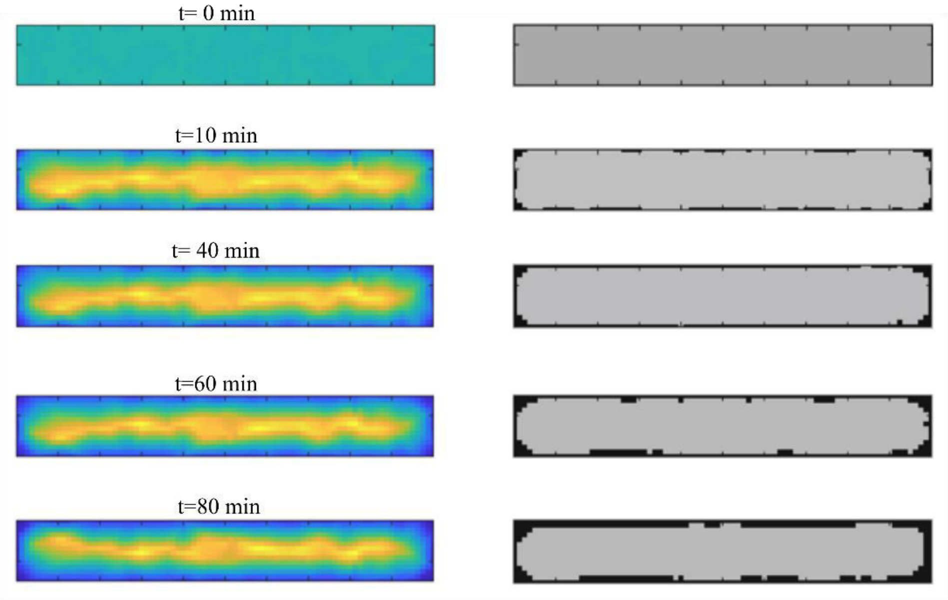


**Figure 16:** The segmentation results of MWT images in the virtual demonstration at different time steps

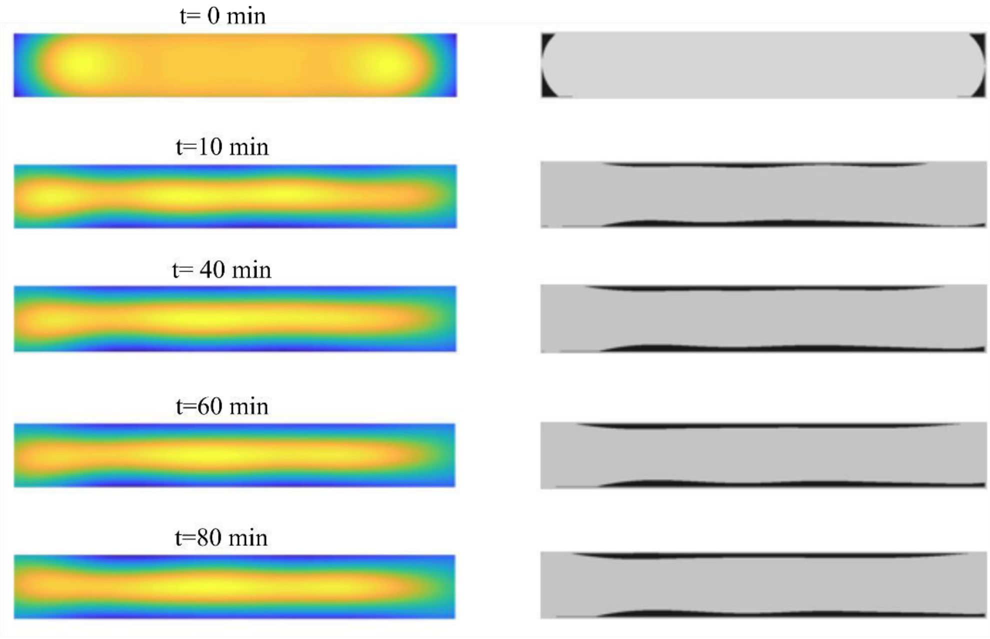


**Figure 17:** The segmentation results of ECT images in the virtual demonstration at different time steps




*This project has received funding from the European Union's Horizon 2020 research and innovation programme under the Marie Skłodowska-Curie Grant Agreement No. 764902.*

# 3. Continuous Casting

## 3.1. Virtual demonstrator design

The basic structure of the virtual controller is shown in Figure 18. Based on OpenFOAM flow simulations all tomographic methods calculate the expected values at the virtual sensors and after adding some noise, the reconstructed image will be given to the controller. Preliminary tests with OpenFOAM revealed that the running time needed for one second of the simulation is approximately one day, since a high spatial discretisation is mandatory in order to resolve the important flow features. Additionally, in the experiment an actuator needs several seconds to finish action, especially in case of the EMBr, where the current through the brake is changed only slowly due to the high inductance. Therefore, it was decided to generate a database containing flow simulations for each action of the controlled variables. Since these simulations are independent, they can be run in parallel. The controller selects a new simulation according to the proposed action of the actuators. Since there exists no reduced order model which describes the effects of the brake on the flow, the large number of different three-dimensional flow simulation is needed.

In the first demonstrator meeting it was agreed that in the first half of the project only single phase flows will be investigated. Hence, the virtual demonstrator will only consider the control of the electromagnetic brake (EMBr) and the control of the gas flow rate will be added later. Therefore, the virtual controller shown in Figure 18 is reduced to the use of CIFT.

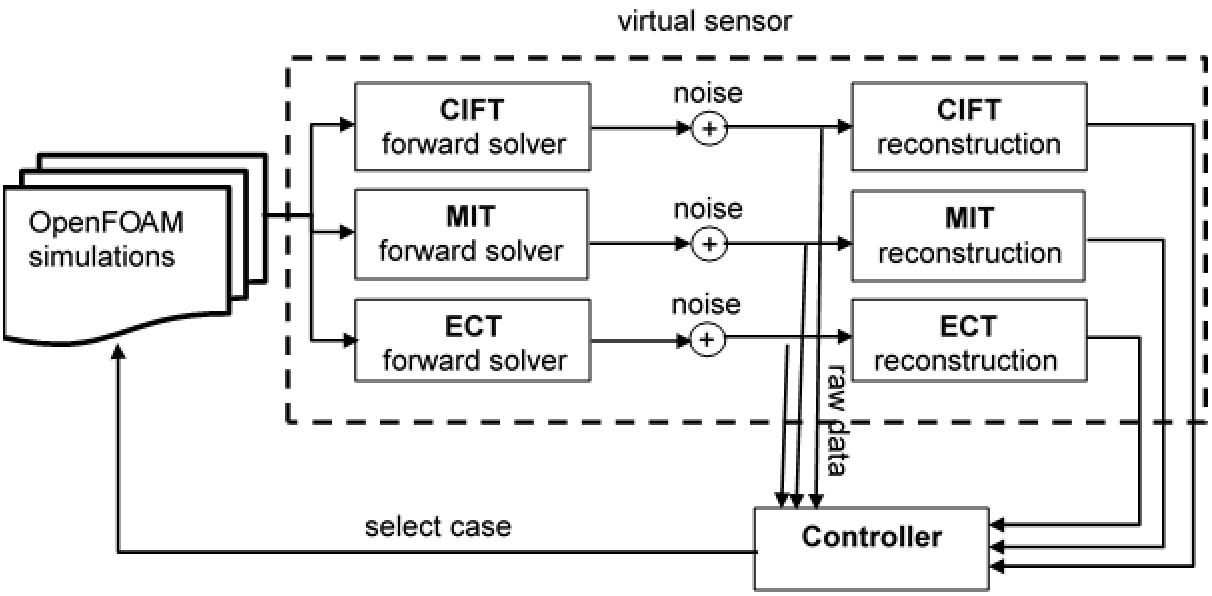


**Figure 18:** Schematic of the virtual controller

However, since the development of the numerical solver took more time as expected and a large number of ultrasound Doppler velocimetry (UDV) measurements of the flow in the demonstrator became available, it was decided to use UDV measurements instead of numerical simulations for the design of the virtual controller. A drawback of this solution is that the





*This project has received funding from the European Union's Horizon 2020 research and innovation programme under the Marie Skłodowska-Curie Grant Agreement No. 764902.*

simulation of CIFT is also not feasible, since the forward solver needs a full three-dimensional flow field in the mould. Therefore, the UDV measurements model the reconstructed flow field by CIFT. It was agreed to switch to the original virtual controller design, when a validated solver for flow simulation is available.

### 3.2. Results of the control loop development

The following preliminary design for the virtual demonstrator will be based on a SISO black box model that will be controlled using Model Predictive Control (MPC). Future plans for the virtual demonstrator will include moving towards a grey box model using the CFD model designed by ESR 5. A closed loop controller will utilize the strength of the EMBr as the manipulated variable. The controlled variable will be the angle of the jet flowing from the submerged entry nozzle (SEN). Tomography sensors should allow us to reconstruct the 3-D velocity fields in the mould, therefore making it possible to calculate the angle using these sensors. The angle is kept within a specific range by the controller in order to prevent a deeper jet impingement into the mould; this allows us to achieve the desirable double roll flow pattern, and to avoid the entrapment of slug.

The SISO model describing the relationship between the EMBr current and the jet angle was obtained using experimental measurements from the Mini-LIMMCAST. Ultrasonic Doppler Velocimetry (UDV) was used in place of the tomographic sensor (Contactless Inductive Flow Tomography); however, the same control methodology will later be implemented with CIFT in the virtual demonstrator, and a comparison between the two sensor techniques will be implemented in order to validate the CIFT-based control loop. In the experimental setup, 10 UDV sensors are used to measure the horizontal velocities in one half of the mould. In order to compute the changing jet angle due to the EMBr, we need to track the movement of the jet. This is done by computing the largest velocities with negative sign measured in the region surrounding the SEN outlet. During every frame captured by the sensors, the algorithm compares the interpolated velocities between the lower five sensors and computes the y-axis position of the most negative velocities. After the most negative velocities have been computed, linear regression using least squares is used to fit a line that would represent the flow of the jet.

Using the above algorithm with the sensor measurements, a model for the system was created using the System Identification Toolbox in MATLAB; specifically process model estimation was used to create the transfer function describing the linear system dynamics. The relationship between the brake current and jet angle can be described by a linear model in the form of a first order model as depicted in Figure 19. It can be observed that there is a good fit between this first order model and the measured data. Moving along to the controller design; the objective of the controller is to maintain the jet angle in the range between 10° and 15° during the operation of the casting process. Additionally, there are constraints on the input current to the EMBr. Due to the above reasons a controller based on Model Predictive Control was used in the control loop. The Model Predictive Control Toolbox in MATLAB was utilized for this step. The most important disturbance affecting the control loop is the nozzle clogging. In one of our simulations we introduce nozzle clogging as a disturbance to our process so that we can assess how efficiently the controller is able to maintain the optimum an-



*This project has received funding from the European Union's Horizon 2020 research and innovation programme under the Marie Skłodowska-Curie Grant Agreement No. 764902.*

gle range, while rejecting the disturbance produced by the nozzle clogging. The clogging disturbance can be modelled as output disturbance because it directly changes the angle of the jet (Cho et al., 2012) [1].

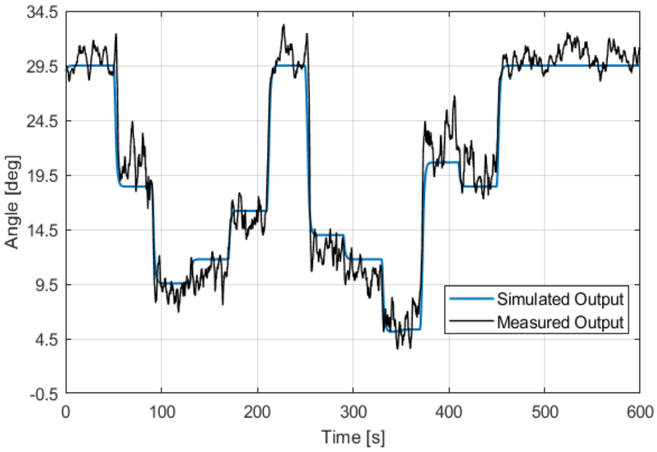


**Figure 19:** Comparison of the simulated model output with the measured output

Two sets of simulations were implemented; the first simulation included set point tracking where we analysed the controller's response to various changes to the set point. Four different set points were used at intervals of t = 20s for this simulation. The controller was able to successfully track the set point with an average settling time of t = 5s. The second set of simulations concentrated on disturbance rejection which is the main concentration of this study. Disturbance due to clogging was introduced at t = 20s which resulted in a gradual increase in the angle response. Furthermore, the effect of unclogging was also introduced at t = 50s which decreased the angle response. In both the clogging and unclogging disturbances, the MPC was able to respond quickly and reject the disturbances in order to maintain the set point reference. We avoided using a more aggressive control effort by the MPC as to avoid reaching saturation in the input control. Furthermore, we implemented open loop control which is generally used in industry, and compared it with our design for the closed loop control, as shown in Figure 20. The simulations show that a closed loop system is needed to prevent the angle from rapidly increasing, and therefore to avoid a deeper jet impingement into the mould due to disturbances such as nozzle clogging. A more detailed description can be found in proceedings of the IFAC Symposium 2019 in South Africa entitled "Control of Jet Flow Angle in Continuous Casting Process using an Electromagnetic Brake".



*This project has received funding from the European Union's Horizon 2020 research and innovation programme under the Marie Skłodowska-Curie Grant Agreement No. 764902.*

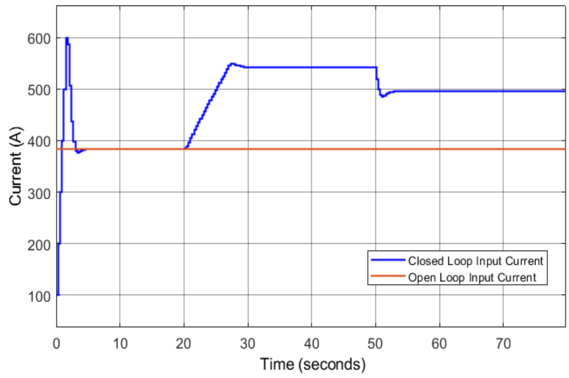


**Figure 20:** Comparison of brake current during disturbance rejection: Closed loop vs. open loop configuration

## 3.3. Implementation of CIFT

For a preliminary OpenFOAM flow simulation, the flow induced magnetic field was calculated, in order to show the working principle of the virtual CIFT sensor. The velocity information in the mould was directly read from the OpenFOAM case, and interpolated into a coarser mesh for CIFT. From the velocity data and the simulated applied magnetic field, a solution to a forward problem is resolved. The calculated flow induced magnetic field for different instances in time is shown in Figure 21. The sensor positions correspond to the position of the sensors at the demonstrator. Data exchange is done via the cloud storage OwnCloud provided by HZDR's IT department.

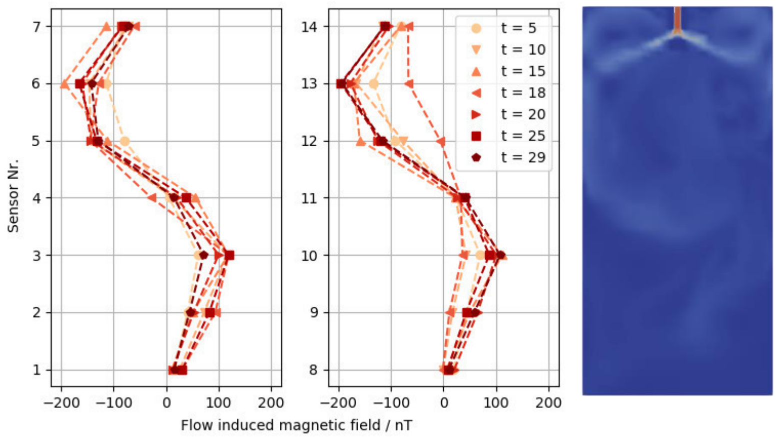


*(a)* *(b)* *(c)*

**Figure 21:** Calculated flow induced magnetic field on the left **(a)** and the right **(b)** narrow side of the mould for a time depended flow simulation and the simulated flow field for t = 15 s **(c)**

## 3.4. References


[1] Cho, S.-M. et al. (2012), Effect of nozzle clogging on surface flow and vortex formation in the continuous casting mold, Iron and Steel Technology, 9, pp. 85–95.





*This project has received funding from the European Union's Horizon 2020 research and innovation programme under the Marie Skłodowska-Curie Grant Agreement No. 764902.*

# 4. Batch Crystallization

## 4.1. Introduction

Crystallization is regarded as the most significant unit operation worldwide that covers various industries such as food, pharmaceutics, biotechnology, cosmetics, etc. Thermodynamics, kinetics, fluid dynamics, crystal structures, and interfacial sciences can be considered as fundamental foundations of crystallization. This process is a combination of particle formation, solid–liquid separation and purification, which can be defined as the formation of a crystalline product out of solution.

From general types of crystallizers, reaction type crystallization (reactive crystallization, precipitation process) is an important unit operation for the formation of solids. In precipitation systems, one of the most significant thermodynamic parameters is supersaturation. It is known as the driving force of the process and results from a chemical reaction as two highly soluble reactants are mixed to form a sparingly soluble product.

Of particular interest is the study of the calcium carbonate crystallization process, which is essential in various industries. Interest in this topic spans in many disciplines such as energy production, paper and cardboard industries, sugar refining process, climate change and carbon capture technology. In these systems, the measurement of nucleation and growth rate as a function of supersaturation is not an easy task since the formation of particles is fast and often hard to control due to a high degree of supersaturation. Hence, new techniques, imaging modalities and algorithms are always required with respect to control and monitoring the processes.

The purpose of this research work is to control and monitor a crystallization process by utilizing new sensing instruments and techniques such as Electrical Resistance Tomography (ERT) and Ultrasound Computed Tomography (USCT). These sensors and reconstruction algorithms are currently under development at Lodz University of Technology, Poland (ESR 11) and University of Bath, UK (ESR 13), respectively. ERT uses the electrical characteristics of the medium for the aim of 3D inverse reconstruction, while sound-speed imaging based on transmission ultrasound tomography is the principle of USCT.

Within this report, the implementation of a traditional PI controller by use of virtual data from 1-D tomographic sensors is described in detail.

## 4.2. Experimental section

### 4.2.1. Semibatch precipitation process of $CaCO_3$

The system of interest is the reaction type crystallization for the semibatch precipitation process of calcium carbonate ($\mathrm{CaCO_3}$) in a highly alkaline solution at an atmospheric pressure (1 atm) and ambient temperature ($21 \pm 2\ °\mathrm{C}$). Small-scale lab experiments were carried out at several operating conditions and the effects of the variation of the agitation rate, feed flow rate and feed concentration on the particle size were investigated. Crystallization occurs by the addition of different concentrations of high-pH carbonate ions ($\mathrm{CO_3^{2-}}$) to an excess amount



*This project has received funding from the European Union's Horizon 2020 research and innovation programme under the Marie Skłodowska-Curie Grant Agreement No. 764902.*

of calcium ions in a water solution. Certain carbonate concentrations are achieved by controlling the pH of water for the $CO_2$ dissolution. The higher boundary of the process window considered in this work is the saturation point of the $CO_2$ dissolution in water at an ambient temperature and pressure, which is 1 mol/lit at pH 12.2.

### 4.2.2. Overview of experimental results and discussion

Accordingly, the precipitation process of calcium carbonate is investigated at three different magnetic stirrer rates namely 50, 300 and 600 RPM. The particle size distribution (PSD) of the final product from each semibatch operation is measured by the laser diffraction method in a particle size analyzer Mastersizer 3000 (Malvern Instruments, UK). As shown in Figure 22, higher mixing rates result in a larger volume mean particle diameter ($D_{43}$). At higher mixing speeds, the reagent distribution (supersaturation) becomes more homogenous which in turn prevents an excessive nucleation. This phenomenon favors the particle growth within the crystallizer. Based on laboratory observations, lower mixing intensities were clearly not able to provide an optimal condition for the distribution of the reagent within the small crystallizer.

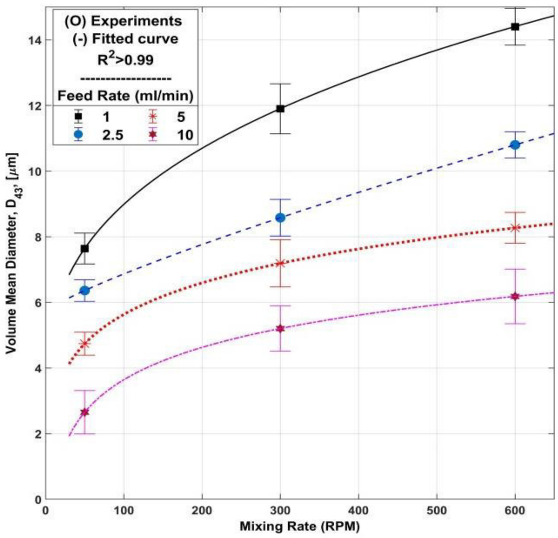


**Figure 22:** Effect of mixing intensity at different feed rates on the average particle diameter during the crystallization process of $CaCO_3$

Moreover, the effect of the feed rate on the average particle diameter for the current reactive crystallization system is also investigated. Crystallization is conducted at the same operating conditions with four different reagent addition rates of 1, 2.5, 5 and 10 ml/min. The addition of the reagent to the crystallizer is controlled by a Masterflex peristaltic pump. Figure 23 represents the effect of the feed rate on $D_{43}$ at various mixing speeds; as shown, the feed rate significantly affects the average particle size.



*This project has received funding from the European Union's Horizon 2020 research and innovation programme under the Marie Skłodowska-Curie Grant Agreement No. 764902.*

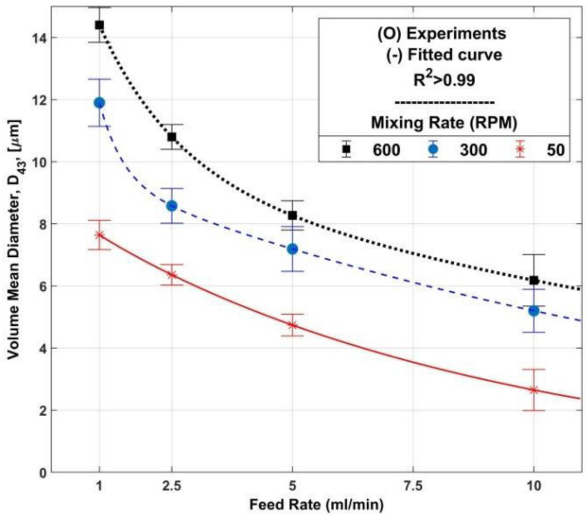


**Figure 13:** Effect of the addition rate at multiple mixing speeds on the average particle diameter during the crystallization process of $CaCO_3$

The crystal lattice analysis through X-ray diffraction is done with a Bruker D8 Advance X-ray diffractometer at LUT University's laboratory. X-ray diffractometry (XRD) determines the atomic and molecular structure of the acquired crystals. Observations based on XRD indicate that the crystal lattice structure of the acquired samples matches well with calcium carbonate. Results of the XRD for one sample at a feed rate of 2.5 ml/min and 600 RPM are shown in Figure 24.

Calcium carbonate appears in three major polymorphic states depending on the precipitation condition: Calcite, aragonite and vaterite; among which only calcite is thermodynamically stable. Depending on the temperature and pH of the solution, each of these polymorphs can be achieved. Investigating the polymorphic state is out of the scope of the current work.

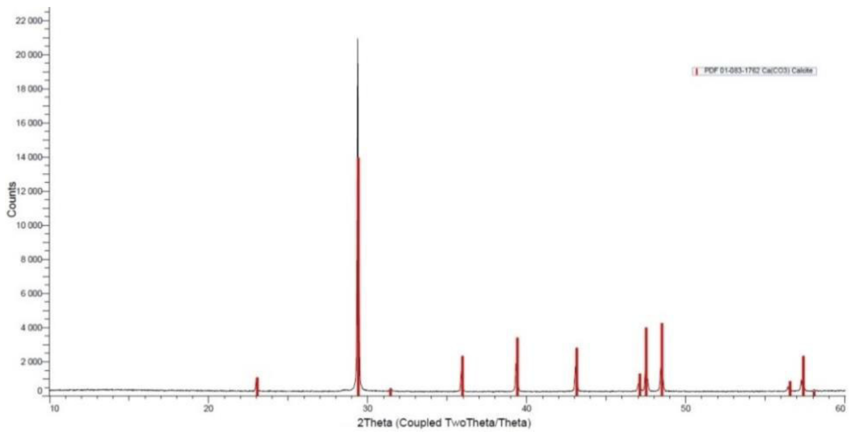


**Figure 24:** X-ray diffraction of a crystallized sample acquired at 2.5 ml/min at 600 RPM





*This project has received funding from the European Union's Horizon 2020 research and innovation programme under the Marie Skłodowska-Curie Grant Agreement No. 764902.*

## 4.3. Process modelling

### 4.3.1. Regression model

The crystallization process is greatly affected by the mixing intensity (mesomixing) and feed flow rate. Mixing at the mesoscale is responsible for concentration distribution and the spreading of solid particles in the crystallizer. On the other hand, the feed rate of the reagent to the receiving tank also plays a significant role on the particle diameter and its final quality. One of these two variables which have the biggest effect on the process output will be used in a control loop to regulate the semibatch crystallization process.

For this purpose, the commercial design of experiments (DOE) software MODDE Pro (Umetrics, Sweden) is utilized to conduct a statistical screening evaluation and extract a regression model that describes the relations between the process inputs (mixing rate, feed rate) and output (mean diameter). For the screening analysis, the fractional design at three levels with five replications of the experiments is used and a Multiple Linear Regression (MLR) approach is applied for the purpose of fitting a model.

Figure 25 shows the graphical representation of basic fit quality factors, where a good model is characterized by these criteria being closer to 1 (100 %). For the current model, R2 (goodness of fit), Q2 (goodness of prediction), model validity and model reproducibility are all in a satisfactory range. Figure 26 displays the coefficient plot as a result of the DOE analysis; the coefficient plot indicates that the feed rate has a more noticeable impact on the average particle diameter during the reactive crystallization process. The size of the coefficient represents the change in the response when a factor varies from 0 to 1. Since the variables are scaled and centered, this makes the coefficient comparison possible.

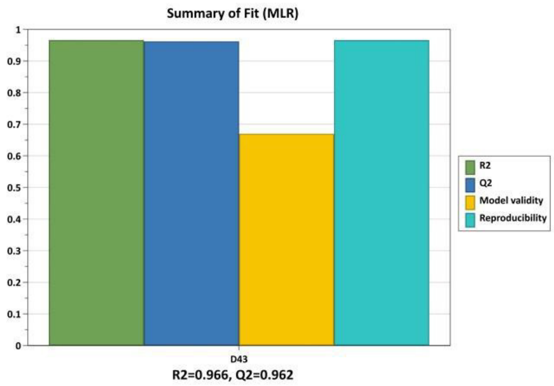


**Figure 25:** Fit quality representation as a result of screening DOE analysis

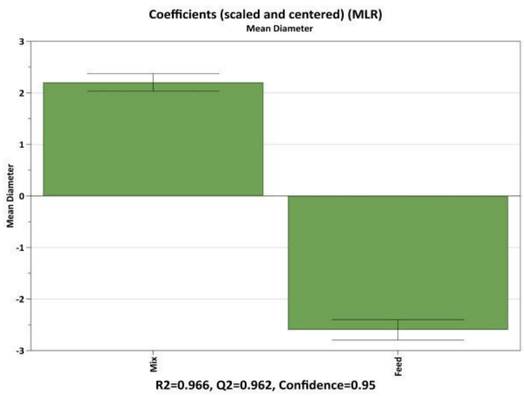


**Figure 26:** Coefficient plot of DOE; size of coefficient represents the change in the response





*This project has received funding from the European Union's Horizon 2020 research and innovation programme under the Marie Skłodowska-Curie Grant Agreement No. 764902.*

Figures 27 and 28 show the normal probability plot of residuals and observed vs. predicted values, respectively. The former indicates that residuals will be located between -4 and +4 standardized standard deviations in case of having a randomly distributed residual; while the latter displays that there is a strong correlation between the model's prediction and its actual outcomes, since all the points are placed close to the 1:1 line.

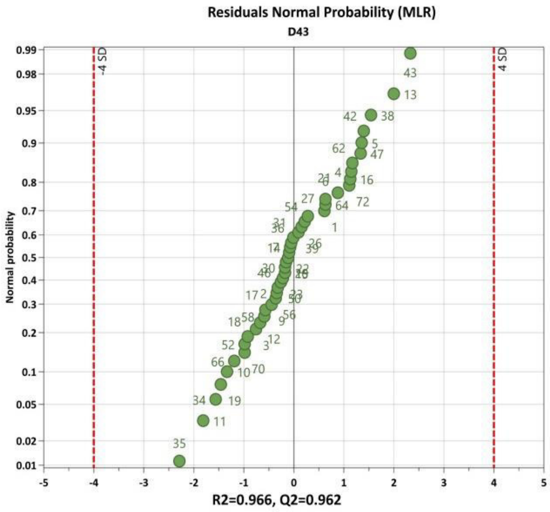


**Figure 27:** Normal probability plot of residuals as a result of screening DOE analysis of experiments

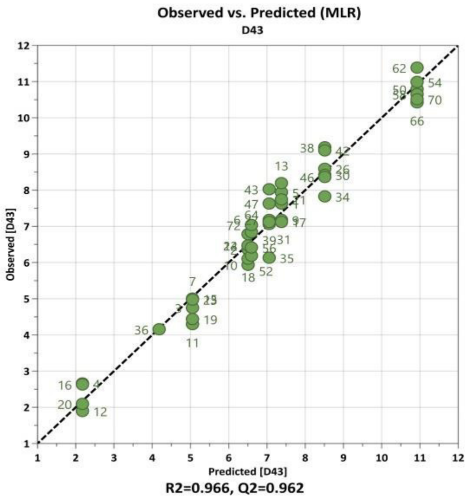


**Figure 28:** Observed versus predicted values of the response

### 4.3.2. System identification

For obtaining a practical mathematical model that describes the process, direct experimental measurements with their fitted data are used instead of utilizing a nonlinear population balance and method of moments approach. Through System Identification methodology within the MATLAB R2019b, a continuous time identified transfer function is extracted that is used for developing a PI controller for a single-input single-output system (SISO); in which the input is the addition rate of the reagent to the crystallizer and the process output is the volume mean diameter. As explained in the previous sections (Figure 26), the process output is relatively more sensitive to a change in the feed rate. Experimental data that are used for model identification are obtained at a mixing speed of 600 RPM for a small-scale crystallizer. This makes it possible to consider an ideally mixed case.

As shown in Figure 29, five sets of experimental data which are obtained at a mixing speed of 600 RPM are selected for developing the model; one separate set of data is used for the model validation.




*This project has received funding from the European Union's Horizon 2020 research and innovation programme under the Marie Skłodowska-Curie Grant Agreement No. 764902.*

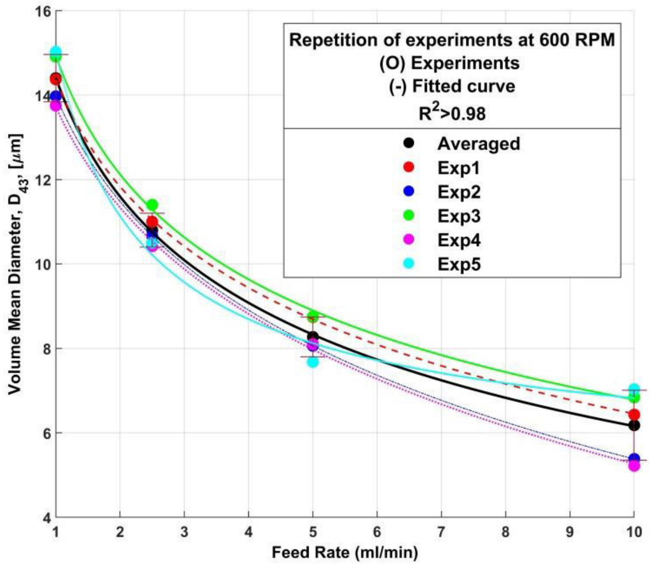


**Figure 29:** Multiple sets of experiments at a mixing intensity of 600 RPM with their fitted curves

## 4.4. Design of the controller

### 4.4.1. PI controller design

The current crystallization process can be controlled by two ways; either by controlling the feed rate or mixing intensity. For the present work, the addition rate of the reagent is used as the manipulated variable. By utilizing Simulink R2019b, a basic PI (proportional–integral) controller is designed to keep the average particle diameter in a desired setpoint. The output mean diameter of the crystallizer is fed back to the controller and the difference between the set point and the measured output is calculated. An actuating signal is generated by the controller as a result of an error signal, which causes the output to reach the desired set point value. A block diagram of the feedback controller is shown in Figure 30.

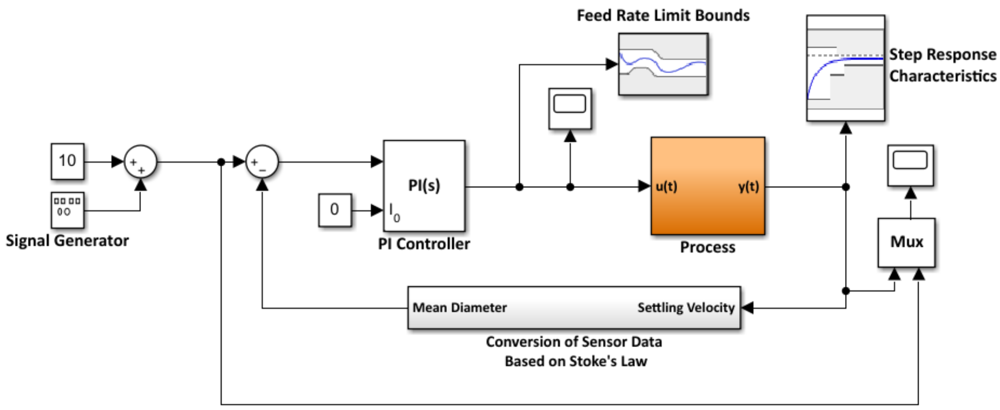


**Figure 30:** Block diagram of a PI controller



*This project has received funding from the European Union's Horizon 2020 research and innovation programme under the Marie Skłodowska-Curie Grant Agreement No. 764902.*

The parameter values for the PI controllers are obtained through optimizing the model response to meet the design requirements, reject disturbances and satisfy the parameter bounds. For this purpose, manipulated variables are subjected to constrains based on the experimental works. Gradient descent, as a first-order iterative optimization algorithm, modifies the variables at each iteration to maintain the response within the design requirement limits.

Multiple set point signals were used to monitor the controller's response to a change in the input. The controller was able to successfully track the set point with a settling time ranging from 110 to 160 s. The response of the PI controller for the set point tracking with the corresponding response of the manipulated variable is shown in Figures 31 and 32.

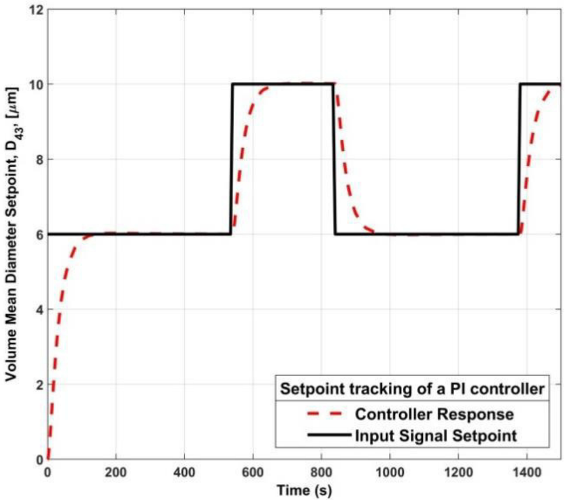


**Figure 31:** PI controller response for set point tracking within the operational bounds of the experiments

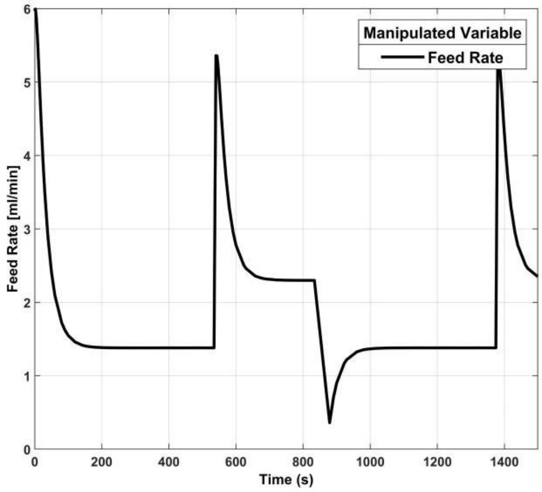


**Figure 32:** Variation in the manipulated variable (feed rate) during the simulation

### 4.4.2. Tomographic sensor data treatment for process control

Measuring and controlling a single particle (5-20 microns) with current tomographic technologies is not feasible and practical. However, tomographic evaluations (electrical resistance tomography or transmission ultrasound tomography) could be correlated to the average particle diameter through the basic principles of fluid mechanics. This section covers the procedures for exploiting the tomographic sensor data to be used in the feedback control loop.

#### 4.4.2.1. Conversion of tomographic data

It is well recognized that in Newtonian fluids, the settling velocity of particles is a function of the free settling velocity (terminal velocity); it decreases as the solid particle concentration increases within the fluid domain. The free settling velocity of particles, $V_t$, is calculated based on the following expression





*This project has received funding from the European Union's Horizon 2020 research and innovation programme under the Marie Skłodowska-Curie Grant Agreement No. 764902.*

$$V_t = \left(\frac{4gd_p(\rho_s - \rho_f)}{3C_D\rho_f}\right)^{1/2} \tag{17}$$

Where, $\rho_f$ and $\rho_s$ are the fluid and solid density, respectively. $d_p$ represents the particle diameter, $g$ is the gravitational acceleration and $C_D$ is the drag coefficient, which is a function of the particle Reynolds number $Re_p$,

$$Re_p = \frac{\rho_f V_t d_p}{\mu} \tag{18}$$

Where $\mu$ denotes the dynamic viscosity of the fluid.

Drag coefficient is a strong function of the hydrodynamic regime of the fluid flow. The corresponding $C_D$ for the spherical particles with an average size ranging from 3 to 10 microns and a Reynolds number between 0.0001 and 0.3, is defined based on Stokes' law

$$C_D = \frac{24}{Re_p} \tag{19}$$

Substituting equation 19 in 17 results in the free settling velocity for the Stokes' regime,

$$V_t = \frac{g{d_p}^2(\rho_s - \rho_f)}{18\mu} \tag{20}$$

it is of utmost importance to check for the fluid flow pattern in order to correlate the drag term since inconsistencies could be very large in case of an error. On the other hand, the presence of other particles affects the value of free settling velocity defined based on Stokes' expression. This phenomenon, known as the hindered settling of particles, occurs because of interactions and the motion of solid particles in suspension within the fluid field.

The deviation between hindered and free settling velocities becomes more pronounced with the increase in the solid volume fraction. Many empirical correlations and mathematical methods have been proposed in the literature for modelling the hindered velocity. A well-known approach is based on the power law function of volume fraction (E. Paul, Handbook of Industrial Mixing: Science and Practice, 2003) as follows

$$V_{HS} = V_t(1 - \phi)^n \tag{21}$$

Where $V_{HS}$ denotes the hindered settling, $\phi$ is the volume fraction and $n$ is the function of the particle Reynolds number as follows: $n = 4.65$ for $Re_p < 0.3$.




*This project has received funding from the European Union's Horizon 2020 research and innovation programme under the Marie Skłodowska-Curie Grant Agreement No. 764902.*

As stated earlier, extreme deviations between the hindered and free settling take place in case of a high solid volume fraction. According to the calculations for the scope of the current work, even with a scale-up to the demo-scale, the solid volume fraction will not exceed 0.05 %, which results in less than 0.005 % error between the hindered settling velocity and the free settling velocity. Therefore, a reasonable assumption has been made to perform the process simulations and actual controller design by employing the Stokes' law during the mathematical modelling.

Accordingly, the idea is to translate the averaged value of tomographic evaluation through the settling velocity $(V_t)$ in a way that it can be used as an input for the controller.

#### 4.4.2.2. Measurement and operational methodology

During the crystallization process, it is expected that the value of resistance (or transmission) will vary due to changes in the suspension density and the settlement of particles. Multiple layers of sensors, which are located at different heights around the reactor, measure these changes through 1-D point-to-point conductivity or sound speed evaluations.

For initiating the process control based on the settling velocity and tomographic measurements, the crystallization process is divided into two phases; that is, operating phase and measurement phase.

The operating phase of the process begins by the addition of a reagent with a predefined rate (based on previous experiments) to the crystallizer equipped with a Hydro Mixer, which results in the formation of preliminary particles. For conducting the measurements using tomographic sensors, both the reagent addition and the mixing completely stop to allow the settlement of particles. During this phase, sensors will monitor the process for any significant change in the characteristics of the medium which is an indicator of the settlement of spherical particles out of the suspension in the crystallizer.

Based on the vertical distance between the sensors and the time of the measurements, the settling velocity is evaluated, and by applying equation 20, the average diameter of the particles could be estimated. In case of a difference between the set point diameter of the controller and the calculated value obtained from the sensors, the controller will apply appropriate corrective actions on the manipulated variable within the next operational loop of the process.

### 4.5. Future work directions

1) Improving the mathematical model to accurately illustrate the process, either through experimental work or linearizing and tuning population balance based on experiments.

2) Investigating the implementation of a Fuzzy Logic Controller or Model Predictive Control. TOMOCON Control Workshop at TU Liberec provided a valuable opportunity to exploit new control approaches.

3) Possible study of image processing to be used in the feedback control loop.



*This project has received funding from the European Union's Horizon 2020 research and innovation programme under the Marie Skłodowska-Curie Grant Agreement No. 764902.*